applied sciences

MDPI

Article

Design and Modelling of a Novel Integrated Photonic Device for Nano-Scale Magnetic Memory Reading

Figen Ece Demirer [1,*,†], Chris van den Bomen [1,†], Reinoud Lavrijsen [1], Jos J. G. M. van der Tol [2] and Bert Koopmans [1]

[1] Department of Applied Physics, Eindhoven University of Technology, 5612 AZ Eindhoven, The Netherlands; chrisvdbomen@gmail.com (C.v.d.B.); r.lavrijsen@tue.nl (R.L.); b.koopmans@tue.nl (B.K.)
[2] Department of Electrical Engineering, Eindhoven University of Technology, 5612 AZ Eindhoven, The Netherlands; J.J.G.M.v.d.Tol@tue.nl
* Correspondence: ecedmrr1@gmail.com
† These authors contributed equally to this work.

Received: 30 October 2020; Accepted: 15 November 2020; Published: 21 November 2020

Featured Application: On-chip optical reading of magnetic memory processed as ultrathin magnetic claddings on photonic waveguides.

Abstract: Design and simulations of an integrated photonic device that can optically detect the magnetization direction of its ultra-thin (∼12 nm) metal cladding, thus 'reading' the stored magnetic memory, are presented. The device is an unbalanced Mach Zehnder Interferometer (MZI) based on InP Membrane on Silicon (IMOS) platform. The MZI consists of a ferromagnetic thin-film cladding and a delay line in one branch, and a polarization converter in the other. It quantitatively measures the non-reciprocal phase shift caused by the Magneto-Optic Kerr Effect in the guided mode which depends on the memory bit's magnetization direction. The current design is an analytical tool for research exploration of all-optical magnetic memory reading. It has been shown that the device is able to read a nanoscale memory bit (400 × 50 × 12 nm) by using a Kerr rotation as small as 0.2°, in the presence of a noise ∼10 dB in terms of signal-to-noise ratio. The device is shown to tolerate performance reductions that can arise during the fabrication.

Keywords: integrated photonics; InP; magneto-optic; MZI; mode conversion; PMA; multi-layered thin film; magnetic memory; MOKE; Fourier transformation

1. Introduction

In the modern world, exponentially increasing generation of data and its handling require novel technologies that perform faster and more energy efficiently. To answer this need, optical components are being used in combination with electronic circuitry to improve the speed and bandwidth of data communication and telecommunication. For example, optical interconnections that were once a conceptual design suggestion [1] are currently being used in commercial products replacing slow and heat-dissipating electrical signal communication channels [2,3]. Researchers continue to demonstrate the superior performance circuitry achieved through the integration of photonics into electronics [4–7]. Yet, these advances require back-and-forth signal conversion between optical and electrical domains, which happens to be the new bottleneck in data communication and processing. Addressing this problem requires establishing novel functionalities in photonic devices that will enable a seamless conversion. Furthermore, (integrated) photonics is lacking a simple and fast non-volatile memory function. A huge potential is anticipated for future devices that enable direct inter-conversion of data between the photonic and magnetic (memory) domain without any intermediate electronics steps,

cutting down on time and energy costs. This study works with existing non-volatile magnetic memory material technology used in electronics: multilayered ferromagnetic thin-film layers. When the multilayered magnetic material is used as memory material, writing bits into the magnetic memory could be facilitated by recent advances in so-called all-optical switching of magnetization [8,9]. Reading out magnetic bits back into the photonic domain could be achieved via a nonreciprocal magneto-optical process [10–12], while dynamic, on-the-fly reading of magnetic bits could be facilitated by racetrack memory concept [9,13]. In a racetrack memory, magnetic domains (memory bits) move while the material that carries the magnetic domains remain stationary [14,15]. Previously, domain wall velocities up to 1000 ms^{-1} were demonstrated [16,17]. It is in this spirit that our paper focuses on the functionality of on-chip optical reading of magnetic memory processed as ultrathin magnetic claddings on photonic waveguides. To our best knowledge, this is the first study which explores the possibility of on-chip, all-optical magnetic memory reading functionality.

State-of-the-art non-volatile magnetic memory such as spin-transfer torque magnetic random-access memory (STT-MRAM) relies on ferromagnetic multilayered ultrathin films with perpendicular magnetic anisotropy (PMA), in which the magnetization vector is perpendicular to the film plane [18]. Such PMA films turn out to be essential for the advanced schemes used to electrically control the magnetic memory elements but are also known for their relatively large magneto-optical efficiency. A simple layer stack that hosts all relevant physical mechanisms is Ta(4)/Pt(2)/Co(1)/Pt(2)/Co(1)/Pt(2) where the numbers in parenthesis are thickness in nm. Bringing this memory component to the proximity of light confined in a waveguide in a photonic device setting gives rise to magneto-optic interactions, specifically the Magneto-optic Kerr Effect (MOKE). MOKE causes a change in the polarization state of light (Kerr rotation and ellipticity), which changes sign when the magnetization direction of the memory component is flipped [11,12]. In a photonic waveguide context, this gives rise to partial mode conversion between TE and TM modes, which potentially enables reading of the memory bit. However, the MOKE signal is intrinsically small in amplitude, a typical Kerr rotation is around 0.05° for films with an in-plane magnetization in free-space optics [19,20]. In order to increase the efficiency of the mode conversion, we propose the use of PMA magnetic claddings, which have not been seriously addressed yet in a photonic perspective. Such claddings with a perpendicular magnetic orientation are expected to display larger amplitude magneto-optical effects, yet still small quantitatively. This calls for developing novel approaches to amplify the magneto-optical effects while showing the importance of on-chip analytical tools to explore the fundamental mode conversion properties of photonic waveguides with PMA claddings.

To assess the feasibility of using MOKE for on-chip all-optical magnetic memory reading functionality, as well as using it as an analytical tool to quantitatively measure magnetization-induced mode conversion, we investigated specially designed photonic devices whose waveguides are cladded with ultra-thin (12 nm), nano-scale (50 × 400 nm) PMA magnetic memory bits, of the composition mentioned before. By using mathematical models of the designed photonic devices, whose building block performance parameters are chosen according to the InP Membrane on Silicon (IMOS) platform [21], the accuracy of the memory-bit read-out, optical loss and tolerance to noise are tested. It has been shown that the device is able to read a nanoscale memory bit (400 × 50 × 12 nm) by using a Kerr rotation as small as 0.2°, in the presence of a ∼10 dB noise in terms of signal-to-noise ratio (SNR). This paper is structured in the following way. In Section 2 materials and methods are given. Device designs, magneto-optic simulation, mathematical modelling and data analysis topics are covered. In Section 3 the results obtained via the mathematical model are presented for devices with varying degrees of performance parameters. A data analysis technique using Fourier transformation is presented. Lastly, in Section 4, the conclusions are given.

2. Materials and Methods

In this section, materials and geometries of the parts that contribute to the overall device are explained. In addition, the device concept, optical simulation and mathematical modelling methods are explained in the subsections.

The material which stores the magnetic information (memory bit) is a multi-layered ferromagnetic metal thin-film structure, whose stack order is given in the previous section. These multi-layers display PMA, where the magnetization vector is perpendicular to the film plane [22]. PMA is highlighted due to its relatively large magneto-optical efficiency [23]. The multi-layers are placed on top of the waveguides as the top cladding. The rest of the photonic device is fabricated on InP membranes since the devices are based on the IMOS platform [21]. The waveguides have a cross-section of 300 $\times$ 400 nm (height and width) and the multi-layered top claddings have the dimensions of 400 $\times$ 50 $\times$ 12 nm (width, length and height).

2.1. Optical Simulation and Device Concept

Before describing the optical simulation method to quantify the MOKE in waveguides, a brief overview is given on MOKE and its impact on the light confined in waveguides. Following this, the devcie concept is introduced.

MOKE is a type of magneto-optic interaction that takes place when the light reflects from a magnetized material. In polar configuration, the effect causes a change in the light's polarization state which is quantified by Kerr rotation and ellipticity (in angles). Typically, in the literature, MOKE is reported for single reflections. Comparing a single reflection case with our work, more interaction, thus a larger MOKE are expected in waveguides with magnetized top claddings. To our best knowledge, there is no prior work that quantifies the Kerr rotation in a waveguide setting. Therefore, finite-difference time-domain (FDTD) simulations [24] of the waveguides with top-claddings are conducted to estimate the MOKE in the guided modes. In the simulation, multi-layer cladding material is defined by using the magneto-optic constant obtained from the literature [25]. It is seen that the Kerr effect causes conversion between TE and TM modes in the waveguide, comparable to the polarization rotation in free-space optics. The resulting Kerr rotation (θ), ellipticity (ϕ) and optical loss ($Loss_{clad.}$) values obtained for a single memory bit are listed in Table 2. These values are used as inputs for the mathematical model explained in Section 2.2.

The device design is done by considering the key enabler of the magnetic memory reading functionality: a change in the sign of the Kerr rotation upon flipping of the magnetization direction of the memory bit (memory bit "1" and "0"). Assuming the confined light is initially in TE mode, the Kerr rotation $\pm\theta$ ($\theta \ll 1$) leads to an emergent TM mode whose field amplitude is proportional to θ for bit 1 and $-\theta$ for bit 0. Therefore, devices which can probe the phase of the emergent TM mode are explored. Mach-Zehnder Interferometers (MZI) are chosen due their ability to convert the phase difference (between the interfering branches) into intensity difference. Balanced and unbalanced MZI are considered as two candidates for the final design. An unbalanced MZI, which has a defined path length difference between the two branches is chosen due to the noise related issues that cannot be addressed in a balanced MZI. This is further elaborated when the presented results are discussed in Section 3. Since at an initial stage, a device is designed for research and exploration purposes, on-chip light source or detector are not considered. To couple an off-chip laser source and an off-chip detector to the device, mode-selective grating couplers are added to the design.

The device design is shown in Figure 1. In this device, TE mode-selective grating coupler is used to couple the light in. Later, a multi-mode interferometer (MMI) is used to split the light equally into two branches. On the upper branch, the TE mode is converted into TM via the polarization converter. The propagation continued (in TM mode) and a delay line is crossed. On the lower branch, the memory bit (magnetic cladding section) caused the TE mode to partially convert into TM mode due to Kerr rotation (θ). The light from the two branches are merged via another MMI. After interference took place, the resulting intensity is picked up via a TM-selective grating coupler.

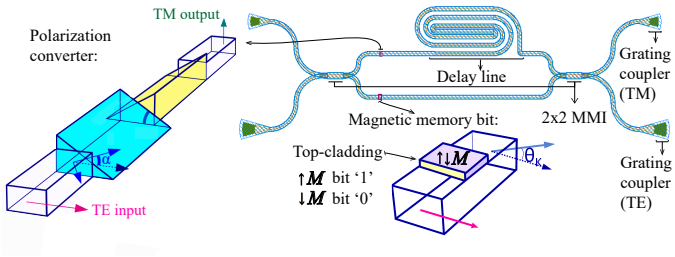

Figure 1. An unbalanced MZI. *TE* and *TM* mode selective grating couplers are used to couple the light in and out. The polarization converter is taken from [26].

2.2. Mathematical Modelling and Fourier Transformation

A mathematical model is built in order to simulate the output light intensity vs. light wavelength for the designed devices. The model is given input parameters that are based on IMOS building block performances [21] and FDTD magneto-optical simulations [24] (see Section 2.1). An overview of the model parameters and their brief descriptions are given in Table 1. Additionally, reduced-performance devices with and without noise are simulated with the model to compare the magnetic memory reading capabilities of the devices. These parameters—some standard for all devices and some changing according to the performance levels—are summarized in Tables 2 and 3, respectively.

Using the mathematical model, equations which determine the electric field (E-field) components of *TE* and *TM* modes in branches 1 and 2, are obtained. For simplicity, coefficients addressing the losses of mode propagations, grating couplers and magnetic cladding are combined into the terms B_n. For description of other parameters please refer to Table 1.

$$\begin{aligned} E_{TE,1} &= B_1 \cos(\alpha)\, e^{-i\frac{2\pi}{\lambda} n_{TE} L_1} \\ E_{TM,1} &= B_2 \sin(\alpha)\, e^{-i\frac{2\pi}{\lambda} n_{TM}(L_1 - x_{\mathrm{PC}})} \\ E_{TE,2} &= B_3 \cos(\theta) e^{-i\frac{2\pi}{\lambda} n_{TE} L_2} \\ E_{TM,2} &= B_4 \sin(\theta) e^{-i\left(\frac{2\pi}{\lambda} n_{TM}(L_2 - x_{\mathrm{clad}}) + \phi\right)}. \end{aligned} \tag{1}$$

Table 1. Overview of model parameters.

Parameters	Definitions
λ	Wavelength scanned (nm)
$Loss_{wg}$	Waveguide propagation loss (assumed to be the same for *TE* and *TM*)
n_{TE}	Effective index of *TE* mode
n_{TM}	Effective index of *TM* mode
L_1	Length of the upper branch (µm)
L_2	Length of the lower branch (µm)
x_{PC}	Distance between polarization converter and left-hand side MMI splitter (µm)
$x_{\mathrm{clad.}}$	Distance between memory bit (cladding) and left-hand side MMI splitter (µm)
$Loss_{clad.}$	Loss due to memory bit (cladding)
$Loss_{GC_{TE\to TE}}$	Loss of *TE*-selective grating coupler for *TE* mode (dB)
θ	Kerr rotation
ϕ	Kerr ellipticity
α	Angle of mode tilt induced by polarization converter (degree)
$Loss_{GC_{TM\to TM}}$	Loss of *TM*-selective grating coupler for *TM* mode (dB)
$Ext_{GC_{TM\to TE}}$	Extinction ratio of *TM*-selective grating coupler for *TE* mode (dB)
Noise	Addition of a Gaussian distribution of random noise to the intensity

Table 2. Showing generic parameters that are valid for all devices.

Parameter	Value
λ	1465–1495 nm
$Loss_{wg}$	3 dB/cm
n_{TE}	2.012
n_{TM}	1.809
Parameter	**Value**
L_1	1386 µm
L_2	462 µm
x_{PC}	200 µm
x_{clad}	100 µm
Parameter	**Value**
$Loss_{clad.}$	0.13 dB/50 nm
$Loss_{GC_{TE\rightarrow TE}}$	1.5 dB
θ	$\pm 0.2^{\circ}$
ϕ	$\pm 0.2^{\circ}$

Table 3. Showing parameters that are dependent on the device performance.

Parameter	Standard Device	Reduced Performance	Noise + Reduced Performance
α	90°	45°	45°
$Loss_{GC_{TM\rightarrow TM}}$	1.5 dB	7 dB	7 dB
$Ext_{GC_{TM\rightarrow TE}}$	50 dB	28 dB	28 dB
Noise	none	none	10.7 dB (SNR)

It is important to recall that the interference takes place between the modes whose E-fields lay in parallel planes and the output light intensity (I) from devices can be calculated via $I = \frac{|E|^2}{2\,Z_0}$, where $|E|$ is the total E-field amplitude and Z_0 is the impedance of the vacuum. The presented equations for E-field amplitudes reveal that a wavelength sweep of the input light will result in oscillations in intensity. Recall that the information regarding the magnetization direction of the cladding (memory bit type) can be retrieved from the sign of the Kerr rotation and ellipticity (θ, ϕ). As seen from the equations above, when TE mode input light is used, information of the memory bit type is visible only in the phase of the TM mode output light. For an output light intensity vs. wavelength plot that is obtained upon interference of both TE and TM modes, two oscillation frequencies, ν_{TE} and ν_{TM} that correspond to these modes are observed.

$$\begin{aligned} \nu_{\mathrm{TE}} &= \frac{n_{\mathrm{TEg}}(L_1 - L_2)}{\lambda^2}, \\ \nu_{\mathrm{TM}} &= \frac{n_{\mathrm{TMg}}(L_1 - L_2 + x_{\mathrm{clad.}} - x_{\mathrm{PC}})}{\lambda^2}. \end{aligned} \tag{2}$$

n_{TEg} and n_{TMg} in Equation (2) indicate group indices of the respective modes. A Fourier transformation can be applied to the resulting output light intensity vs. wavelength data to separate the TM mode contribution. Thanks to this technique, the amplitude and phase of the TM mode component can be found. In order to separate the TE and TM mode contributions, non-overlapping peaks in the Fourier transform is required. Therefore, at the design stage, it is vital to choose $x_{\mathrm{clad.}}$ and x_{PC} parameters (see Table 1) accordingly.

3. Results and Discussion

In order to demonstrate the magnetic memory reading capabilities of our devices, the mathematical model described in Section 2.2 was used. As explained in Section 2.1, the chosen

devices were unbalanced interferometers that contain built-in ferromagnetic memory components as their top claddings. The model predicted the output light intensity vs. wavelength plots of the devices with opposing memory bits (bit '1' and '0'). Later these plots were analyzed by the Fourier transformation technique to determine the memory bit type, thus realize 'reading' of the magnetic information. Recall that since the magneto-optic interaction which enables the determination of the memory bit type is only extractable from the phase of the TM mode (when TE mode is used as input), Fourier technique greatly reduced the noise and enhanced the sensitivity.

In Figure 2, the left column plots present output light intensity vs. wavelength data. Note that plots depict the intensity after a windowing function is applied. The right column plots show the Fourier transformation of the left column in blue color and the phase difference between two memory bit states for each oscillatory components in red color. Figure 2a,c,e represent the standard, reduced-performance and noisy reduced-performance devices, respectively. The standard device shown in Figure 2a demonstrate a clear 180° phase shift between the two signals which correspond to the opposite memory states. The Fourier transformation in Figure 2b (right side y-axis) show a single peak which correspond to the TM mode (see Equation (2)). The fact that there is only TM mode is thanks to the well-performing TM-selective out-couplers in the standard devices that have a negligible out-coupling of the TE mode. As expected, the phase difference plot in Figure 2b (left side y-axis) indicate 180° difference at the region which correspond to TM peak. Note that the plots depicting phase difference between two memory states convey meaningful information only at the locations where a correspondent Fourier peak is present. To stress this aspect visually in the graph, the points corresponding to a peak are shown in black, whereas the rest is left grey. In Figure 2c, the 'reduced-performance device' is seen. This device has only 45° conversion at the polarization converter and the TE-mode couples out from the TM-selective out-coupler (see Table 3). Due to coupling out of the TE mode that does not carry information on the memory bit's state, it impossible to observe a 180° phase shift in the intensity vs. wavelength plot upon a change in the memory bit type. As expected, Figure 2d reveals two Fourier peaks that correspond to TE and TM modes. As seen from the peak intensities, despite the use of TM-selective out-couplers, the TE mode dominates. Undeterred by the TE mode dominance, the phase difference plot in Figure 2e indicates a phase of 180° at the position corresponding to the TM peak. The phase shift corresponding to the TE mode reads 0°. Testing the device design further by addition of a noise that described in Section 2.2, Figure 2e,f are obtained. The 'noisy and reduced-performance device' demonstrates that, even though the intensity vs. wavelength plot is dominated by noise and mixed modes, it is still possible to determine the magnetic memory type via the Fourier transform technique.

Referring back to Section 2.1 and clarifying the reason for the choice of an unbalanced MZI design over a balanced one, as seen in Figure 2a, if the device is performing at a fixed wavelength, the change in the light intensity upon changing the memory bit type corresponds to only 0.3% of the total light intensity. This observation indicates that the magnetic memory reading functionality of the device can be obstructed by the noise when operating at a single wavelength. Sweeping of a range of wavelengths accompanied by the Fourier transformation method are the key concepts for eliminating sensitivity to noise and increasing memory reading accuracy. Since the wavelength sweep technique is not successful without the specific frequency oscillations that the added delay line provides, an unbalanced MZI is preferred over a balanced one.

Note that for an ideal device depicted in Figure 2a, the difference in light intensity between the two memory states is proportional to the strength of the Kerr rotation. Therefore, if a calibration by using a material with known Kerr rotation and optical loss is done, very small Kerr rotations can be measured quantitatively by using the same design.

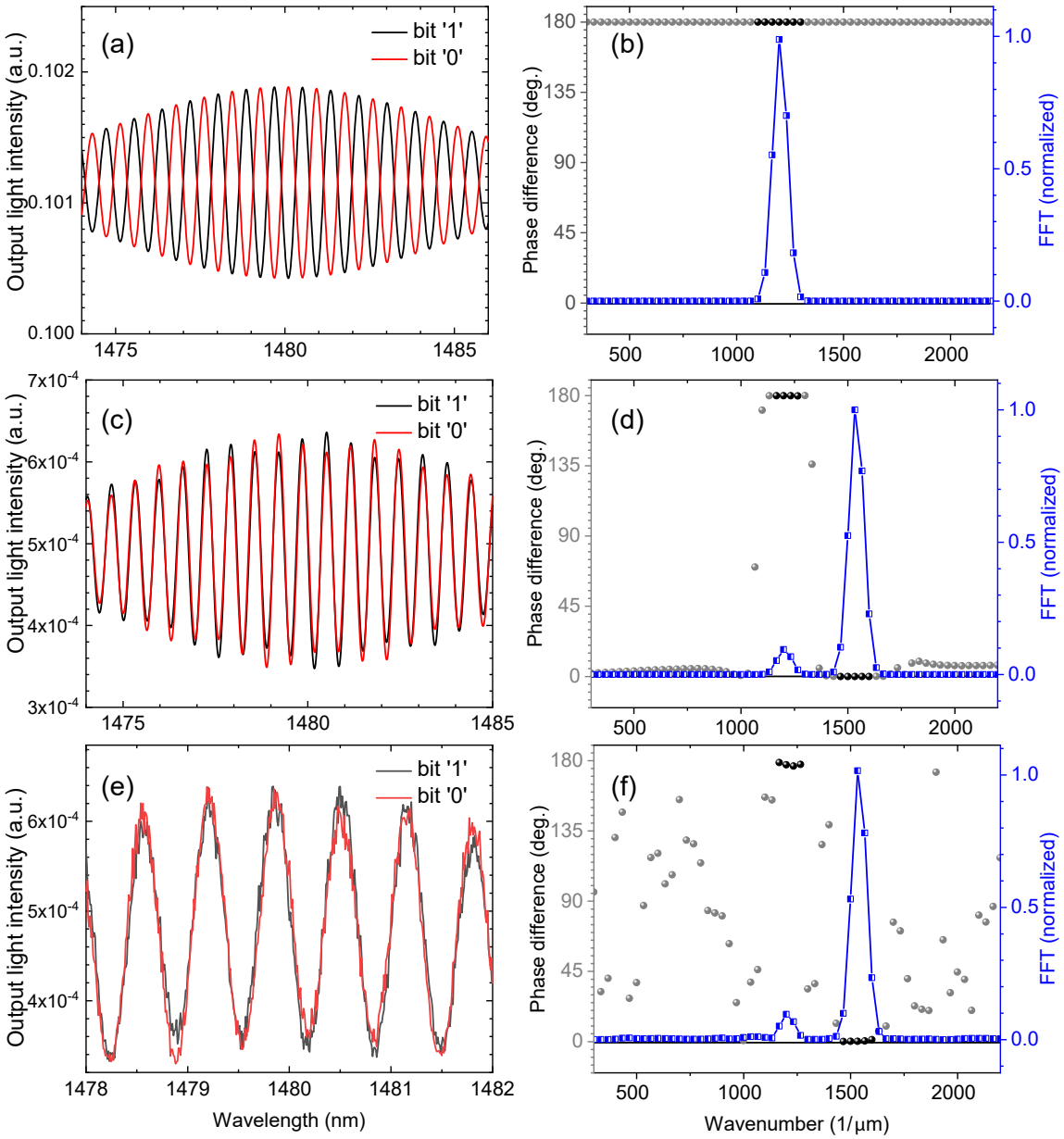

Figure 2. (**a**,**c**,**e**) Output light intensity vs. wavelength plots for standard, reduced-performance, and noisy reduced-performance devices (see Tables 2 and 3), The light intensities are shown in arbitrary units and is normalized assuming initial intensity (I_0) is 1. (**b**,**d**,**f**) In blue, Fourier transformations of the intensity vs. wavelength plots are shown. The normalization is done assuming the highest intensity Fourier peak has amplitude 1. In black, the phase differences between the memory bit "1" and "0" are shown for each wavenumber. The data-points which correspond to a Fourier peak are shown in black while the rest is shown in grey. This is done for guidance to eye for separation of statistically significant result (black) and fitting procedure noise (grey).

4. Conclusions

An integrated photonic device specially designed to perform memory reading functionality is presented. The functionality is achieved through detection of the magnetization direction of an ultra-thin memory bit. The device is shown to operate despite performance reductions in the contributing building blocks and noise levels which correspond to ∼10 dB in terms of SNR. Post-processing of the intensity signal via Fourier transformation method stressed that the device is suitable as an analytical tool for research purposes. It is highlighted that the quantitative measurement

of very small magneto-optic Kerr rotation (0.2°) is possible after a calibration which also considers optical loss.

Author Contributions: F.E.D. designed and directed the project, did FDTD simulations, contributed to the interpretation of the results and took the lead in writing the manuscript. C.v.d.B. developed the mathematical model, obtained and analyzed the results and prepared a draft manuscript. R.L. aided in interpreting the results, helped with methodology and provided input on the structure of the manuscript. J.J.G.M.v.d.T. and B.K. supervised the project, provided conceptualization of the work and reviewed/edited the work. All authors provided critical feedback and helped shape the research, analysis and manuscript. All authors have read and agreed to the published version of the manuscript.

Funding: This work is part of the Gravitation program 'Research Centre for Integrated Nanophotonics', which is financed by the Netherlands Organisation for Scientific Research (NWO).

Conflicts of Interest: The authors declare no conflict of interest.

References

1. Goodman, J.W.; Leonberger, F.J.; Kung, S.-Y.; Athale, R.A. Optical interconnections for VLSI systems. *Proc. IEEE* **1984**, *72*, 850–866. [CrossRef]
2. A Record Breaking Optical Chip. Available online: https://www.technologyreview.com/2008/06/25/219782/a-record-breaking-optical-chip/ (accessed on 11 November 2020).
3. Intel Leverages Chip Might Etch Photonics Future. Available online: https://www.nextplatform.com/2016/08/17/intel-leverages-chip-might-etch-photonics-future/ (accessed on 11 November 2020).
4. Kish, F.; Lal, V.; Evans, P.; Corzine, S.W.; Ziari, M.; Butrie, T.; Reffle, M.; Tsai, H.S.; Dentai, A.; Pleumeekers, J.; et al. System-on-chip photonic integrated circuits. *IEEE J. Sel. Top. Quantum Electron.* **2017**, *24*, 1–20. [CrossRef]
5. Sun, C.; Wade, M.T.; Lee, Y.; Orcutt, J.S.; Alloatti, L.; Georgas, M.S.; Waterman, A.S.; Shainline, J.M.; Avizienis, R.R.; Lin, S.; et al. Single-chip microprocessor that communicates directly using light. *Nature* **2015**, *528*, 534–538. [CrossRef] [PubMed]
6. Atabaki, A.H.; Moazeni, S.; Pavanello, F.; Gevorgyan, H.; Notaros, J.; Alloatti, L.; Wade, M.T.; Sun, C.; Kruger, S.A.; Meng, H.; et al. Integrating photonics with silicon nanoelectronics for the next generation of systems on a chip. *Nature* **2018**, *556*, 349–354. [CrossRef]
7. Smit, M.; Williams, K.; Van Der Tol, J. Past, present, and future of InP-based photonic integration. *APL Photonics* **2019**, *4*, 050901. [CrossRef]
8. Stanciu, C.; Hansteen, F.; Kimel, A.; Kirilyuk, A.; Tsukamoto, A.; Itoh, A.; Rasing, T. All-optical magnetic recording with circularly polarized light. *Phys. Rev. Lett.* **2007**, *99*, 047601. [CrossRef]
9. Lalieu, M.; Peeters, M.; Haenen, S.; Lavrijsen, R.; Koopmans, B. Deterministic all-optical switching of synthetic ferrimagnets using single femtosecond laser pulses. *Phys. Rev. B* **2017**, *96*, 220411. [CrossRef]
10. Van Hees, Y.; van der Tol, J.; Koopmans, B.; Lavrijsen, R. Periodically modulated ferromagnetic waveguide claddings with perpendicular magnetic anisotropy for enhanced mode conversion. *IEEE Photonics Benelux Proc.* **2017**, 196–199. Available online: http://www.photonics-benelux.org/images/stories/media/proceedings/2017/s17p196.pdf (accessed on 21 November 2020).
11. Kerr, J. On rotation of the plane of polarization by reflection from the pole of a magnet. *Lond. Edinb. Dublin Philos. Mag. J. Sci.* **1877**, *3*, 321–343. [CrossRef]
12. Freiser, M. A survey of magnetooptic effects. *IEEE Trans. Magn.* **1968**, *4*, 152–161. [CrossRef]
13. Parkin, S.S.; Hayashi, M.; Thomas, L. Magnetic domain-wall racetrack memory. *Science* **2008**, *320*, 190–194. [CrossRef]
14. Ryu, K.S.; Thomas, L.; Yang, S.H.; Parkin, S.S. Current induced tilting of domain walls in high velocity motion along perpendicularly magnetized micron-sized Co/Ni/Co racetracks. *Appl. Phys. Express* **2012**, *5*, 093006. [CrossRef]
15. Yang, S.H.; Ryu, K.S.; Parkin, S. Domain-wall velocities of up to 750 m s- 1 driven by exchange-coupling torque in synthetic antiferromagnets. *Nat. Nanotechnol.* **2015**, *10*, 221–226. [CrossRef] [PubMed]
16. Caretta, L.; Mann, M.; Büttner, F.; Ueda, K.; Pfau, B.; Günther, C.M.; Hessing, P.; Churikova, A.; Klose, C.; Schneider, M.; et al. Fast current-driven domain walls and small skyrmions in a compensated ferrimagnet. *Nat. Nanotechnol.* **2018**, *13*, 1154–1160. [CrossRef] [PubMed]

17. Franken, J.; Swagten, H.; Koopmans, B. Shift registers based on magnetic domain wall ratchets with perpendicular anisotropy. *Nat. Nanotechnol.* **2012**, *7*, 499–503. [CrossRef] [PubMed]
18. Wang, M.; Zhang, Y.; Zhao, X.; Zhao, W. Tunnel junction with perpendicular magnetic anisotropy: Status and challenges. *Micromachines* **2015**, *6*, 1023–1045. [CrossRef]
19. Fiedler, S.; Stillrich, H.; Oepen, H.P. Magneto-optic properties of electron cyclotron resonance ion beam sputtered and magnetron sputtered Co/Pt multilayers. *J. Appl. Phys.* **2007**, *102*, 083906. [CrossRef]
20. Krinchik, G.S.; Artemjev, V.A. Magneto-optic Properties of Nickel, Iron, and Cobalt. *J. Appl. Phys.* **1968**, *39*, 1276–1278. [CrossRef]
21. Van der Tol, J.J.G.M.; Jiao, Y.; Van Engelen, J.P.; Pogoretskiy, V.; Kashi, A.A.; Williams, K. InP Membrane on Silicon (IMOS) Photonics. *IEEE J. Quantum Electron.* **2020**, *56*, 1–7. [CrossRef]
22. Lavrijsen, R.; Hartmann, D.M.F.; van den Brink, A.; Yin, Y.; Barcones, B.; Duine, R.A.; Verheijen, M.A.; Swagten, H.J.M.; Koopmans, B. Asymmetric magnetic bubble expansion under in-plane field in Pt/Co/Pt: Effect of interface engineering. *Phys. Rev. B* **2015**, *91*, 104414. [CrossRef]
23. Višňovskỳ, Š.; Jakubisová Lišková, E.; Nỳvlt, M.; Krishnan, R. Origin of magneto-optic enhancement in CoPt alloys and Co/Pt multilayers. *Appl. Phys. Lett.* **2012**, *100*, 232409. [CrossRef]
24. Lumerical Solutions. Available online: https://www.lumerical.com/products/ (accessed on 29 October 2020).
25. Atkinson, R.; Pahirathan, S.; Salter, I.W.; Grundy, P.J.; Tatnall, C.J.; Lodder, J.C.; Meng, Q. Fundamental optical and magneto-optical constants of CoPt and CoNiPt multilayered films. *J. Magn. Magn. Mater.* **1996**, *162*, 131–138. [CrossRef]
26. Pello, J.; van der Tol, J.; Keyvaninia, S.; van Veldhoven, R.; Ambrosius, H.; Roelkens, G.; Smit, M. High-efficiency ultrasmall polarization converter in InP membrane. *Opt. Lett.* **2012**, *37*, 3711–3713. [CrossRef] [PubMed]